Microelectronics Reliability 51 (2011) 1525–1529

Contents lists available at ScienceDirect

Microelectronics Reliability

journal homepage: www.elsevier.com/locate/microrel

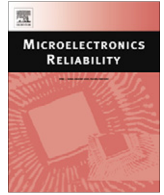

# An analytical approach for physical modeling of hot-carrier induced degradation

S. Tyaginov [a,b,*], I. Starkov [c], H. Enichlmair [d], Ch. Jungemann [e], J.M. Park [d], E. Seebacher [d], R. Orio [a], H. Ceric [c], T. Grasser [a]

[a] Institute for Microelectronics, TU Wien, Gußhausstraße 27-29, A-1040 Vienna, Austria
[b] A.F.Ioffe Physical–Technical Institute, 26 Polytechnicheskaya Str., 194021 St.-Petersburg, Russia
[c] Christian Doppler Laboratory for Reliability Issues in Microelectronics at IUE, TU Wien, Gußhausstraße 27-29, A-1040 Vienna, Austria
[d] Austriamicrosystems AG, Unterpremstätten, Austria
[e] Institute für Theoretische Elektrotechnik, RWTH Aachen, Germany

ARTICLE INFO

*Article history:*
Received 9 June 2011
Received in revised form 30 June 2011
Accepted 5 July 2011
Available online 11 August 2011

ABSTRACT

We develop an analytical model for hot-carrier degradation based on a rigorous physics-based TCAD model. The model employs an analytical approximation of the carrier acceleration integral (calculated with our TCAD approach) by a fitting formula. The essential features of hot-carrier degradation such as the interplay between single-and multiple-electron components of Si–H bond dissociation, mobility degradation during interface state build-up, as well as saturation of degradation at long stress times are inherited. As a result, the change of the linear drain current can be represented by the analytical expression over a wide range of stress conditions. The analytical model can be used to study the impact of device geometric parameters on hot-carrier degradation.

© 2011 Elsevier Ltd. All rights reserved.

## 1. Introduction

It is commonly acknowledged that a reduction of device dimensions is accompanied by a change of the hot-carrier degradation (HCD) worst-case conditions. The physical reason behind this tendency is the change of the Si–H bond-breakage mechanism [1–4]. While in long-channel and/or high-voltage devices the bond dissociation is triggered by the single-particle process, in ultra-scaled MOSFETs the multiple-particle process is responsible for the interface state creation. Note that the first mechanism is associated with high-energy carriers which are called “hot”. In contrast, the multiple-particle process implies a series of interactions between the bond and “colder” particles. However, as we showed in our previous works, even in the case of high voltage 5 V n-MOSFETs with an effective channel length of 0.5 μm the latter process still plays a significant role [5,6]. Therefore, both competing components are present in a real device and the information how these mechanisms contribute to the defect build-up is provided by the carrier energy distribution function, which determines the carrier acceleration integral (AI) [7,8,2,3,5,6].

One of the manifestations of HCD is the linear drain current $I_{\mathrm{dlin}}$ degradation. The $I_{\mathrm{dlin}}$ change with time is a consequence of a large number of microscopic contributions. These contributions are related to the dangling bonds produced due to the Si–H bond dissociation. A dangling bond can capture a carrier, thereby producing a charged defect, which perturbs the electrostatics of a device and degrades the mobility. The driving force of the bond-breakage process is the energy deposited by carriers and thus the distribution of the energy describes the intensity of the bond dissociation mechanism. At the same time, the carrier ensemble evolves as it moves through the device. Physically this means that the carrier distribution function (and the acceleration integral) changes with the coordinate along the interface. Since the acceleration integral defines the characteristic time for trap creation, the interface states are distributed spatially and over the characteristic time. This time, in turn, describes the activation exponent and thus the dynamics of defect creation process.

The analogous situation is typical for negative bias temperature instability where the dispersion of time constants (describing defect activation) stems from the distribution of the activation energy [9–11]. The mathematical formalism for this case was elaborated using the Fermi–Dirac function derivative as probability density for the activation energy. This shape of the distribution leads to a power law dependence of the degrading parameter, see [7,12,13]. In the case of HCD the situation is more complicated because the activation of Si–H bond dissociation process is triggered by the AI which is coordinate dependent [5,6]. The bonds located at the coordinate corresponding to a smaller value of the AI will be broken later than those located near the drain end of the gate, i.e. near the typical AI peak [5,6]. Therefore, one should consider the matter in terms of the distribution of the acceleration integral $I(x)$ with the lateral coordinate $x$.

Based on our TCAD model for HCD [5,6] we fit the acceleration integral with an analytical formula. Such an approach allows us to

* Corresponding author at: Institute for Microelectronics, TU Wien, Gußhausstraße 27-29, A-1040 Vienna, Austria. Tel.: +43 1 58801 36025; fax: +43 1 58801 36099.
*E-mail address:* tyaginov@iue.tuwien.ac.at (S. Tyaginov).

0026-2714/$ - see front matter © 2011 Elsevier Ltd. All rights reserved.
doi:10.1016/j.microrel.2011.07.089

express the interface state density $N_{it}$ and, hence, the degradation of the linear drain current analytically. The crucial peculiarity of this concept is that it is based on the physical principles behind HCD rather than on empirical fitting of experimental data. In particular, this means that the interplay between the single- and multiple-carrier mechanisms of the defect creation is considered by the model. This is very important because HCD tests are performed at accelerated conditions where carriers are rather hot. At real operation conditions, however, the voltages are lower and thus are the carrier energies. As a consequence, the role of the multiple-particle process is accelerated. Therefore, under real operation conditions the relative contribution of the latter mechanism is expected to be increased and the transition from stress to operating conditions may only be captured by a physics-based HCD model.

## 2. Experimental and TCAD support

For this work we used high voltage 5 V n-MOSFETs (sketched in Fig. 1) designed on a standard 0.35 μm technology. To ensure such a high operating voltage a thicker gate oxide (with an oxide thickness of 15 nm), a longer channel thickness and special measures concerning the source/drain doping were taken. The devices have been subjected to hot-carrier stress for $10^4$ s at room temperature, using the gate voltage $V_{gs}$ = 2.0 V and 5 different drain voltages $V_{ds}$ = 6.25, 6.5, 6.75, 7.0, 7.25 V. To calculate the carrier distribution function we employed our TCAD model for hot-carrier degradation [5,6]. This model relies on the carrier transport treatment by means of a full-band Monte-Carlo device simulator MONJU [14]. MONJU is used to calculate the carrier DF for a particular device architecture, for given stress conditions and at arbitrary position inside the transistor. A typical shape of the $I(x)$ profile (calculated for $V_{ds}$ = 7.25 V) is represented in Fig. 2. This information will be further used as an additional "experimental" input. Moreover, the information on $I(x)$ is crucial for the derivation of the analytical model because it will be based on fitting of this profile by an analytical expression.

## 3. Analytical model

The linear drain current degradation due to $N_{it}$ build-up is [3]:

$$\Delta I_{dlin}/I_{dlin0} = \Delta V_t/(V_{gs} - V_t) + \Delta\mu/\mu_0, \quad (1)$$

where $I_{dlin0}$ and $\mu_0$ are the linear drain current and mobility of the fresh device, $V_t$ is the threshold voltage, $\Delta\mu(\Delta V_t)$ is the change in

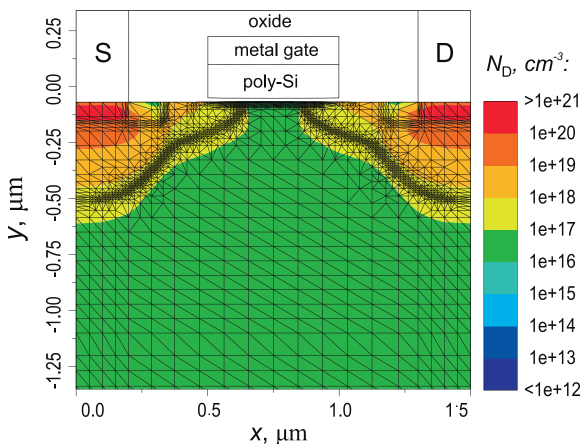


**Fig. 1.** The sketch of the 5 V n-MOSFET used in this work. The phosphorous doping concentration is represented by the color map while the source/drain contacts are marked as "S" and "D", respectively. The origin of the lateral coordinate corresponds to the beginning of the source.

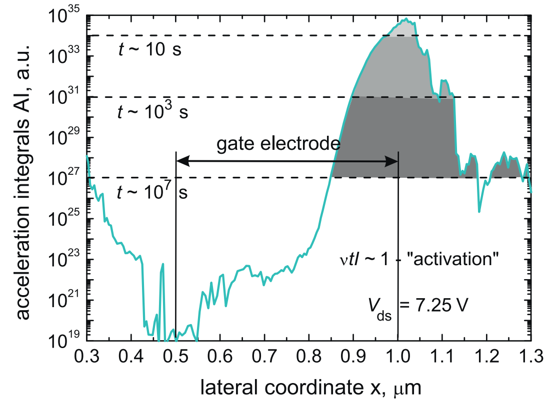


**Fig. 2.** An example of the TCAD result for the AI with characteristic activation times being sketched.

mobility (threshold voltage). The mobility of the degraded device is calculated as [15–17]:

$$\mu = \mu_0/(1 + \alpha_{sc}N_{it}), \quad (2)$$

where $\alpha_{sc}$ is a prefactor. Further throughout the paper under $\Delta I_{dlin}$ we understand its relative value (in percents), i.e. switch from $\Delta I_{dlin}$ to $\Delta I_{dlin}/I_{dlin0}$. Relying on the experimental observations that in our device $\Delta V_t$ is weak, we link $\Delta I_{dlin}$ and $N_{it}$:

$$\Delta I_{dlin} = \alpha_{sc}N_{it}/(1 + \alpha_{sc}N_{it}). \quad (3)$$

As in the TCAD version we consider two competing mechanisms for Si–H bond-breakage, i.e. the single-electron (SE-) and multiple-electron (ME-) processes [3,5,6]. The interface states generated by the SE-process are characterized by the density $N_{it,SE}$ which is found by assuming first-order kinetics for the bond-breakage reaction [2,5]:

$$N_{it,SE}(t,x) = N_0[1 - e^{-t\nu I(x)}], \quad (4)$$

where $\nu = 5 \times 10^{-35}$ a dimensionless coefficient (the combination of physical parameters from the TCAD model). As for the ME-induced defects, their concentration is calculated considering the Si–H bond as a truncated harmonic oscillator [3,5,6]:

$$N_{it,ME}(t,x) = N_0\left(\frac{\lambda_{ME}}{P_{pass}}\left(\frac{\eta I(x) + w_e \exp(-\hbar\omega/k_B T_L)}{\eta I(x) + w_e}\right)^{N_l}\right)^{1/2} \times [1 - \exp(-\lambda_{ME}t)]^{1/2}, \quad (5)$$

where $N_0$ is the total concentration of both passivated and depassivated Si–H bonds, the rates $\lambda_{ME}$ and $P_{pass}$ describes hydrogen jumping from the last bonded to the transport state and back [3,5,6]. The prefactor $\eta$ is similar to $\nu$ for the SE-process. The phonon frequency $w_e$, the distance between the oscillator levels $\hbar\omega$ and the number of eigenstates in the quantum well $N_l$ are characteristics of the bond energetics while $k_B$ is the Boltzmann constant and $T_L$ the lattice temperature. As shown in [5,6], the ME-related contribution is not coordinate-dependent because the acceleration integral reaches high values, thereby saturating the prefactor $(\eta I(x) + w_e \exp(-\hbar\omega/k_B T_L)/(\eta I(x) + w_e)$. Thus, we do not consider the density $N_{it,ME}$ as a spatially distributed quantity.

Since we are striving to develop an analytical model which does not use any information from the TCAD version (e.g. lateral profiles such as $N_{it}(x)$ and $I(x)$), for the SE-process we introduce the average (over the interface) trap concentration:

$$\overline{N}_{it,SE} = N_0\left[1 - \frac{1}{x_{max} - x_{min}}\int_{x_{min}}^{x_{max}} e^{-t\nu I(x)}\,dx\right], \quad (6)$$

with $x_{max}$, $x_{min}$ as the boundaries of the $Si/SiO_2$ interface. The integration over $x$ captures all values of the AI. The probability that a S–H bond is broken within a certain time slot is given by (4). The coordinate-dependent acceleration integral $I(x)$ defines the characteristic time of defect creation for each particular position along the interface.

Fig. 2 shows the AI profile $I(x)$ for $V_{ds}$ = 7.25 V which can be decomposed onto two parts, i.e. the linear dependence (on a log-scale) on the coordinate $I_{linear}$ and the peak $I_{peak}(x)$, see Figs. 2 and 4:

$$I(x) = I_{linear}(x) + I_{peak}(x),$$
$$I_{linear} = A_1 \exp(\alpha(x - x_{min})), \tag{7}$$

The decaying line observed in the range 0.3–0.5 μm can be omitted because only bonds where the condition $\nu t I \sim 1$ is satisfied have a significant probability to be broken; i.e. this fragment corresponds to $t > 10^7$ s and the dissociation process is not triggered within the given time slot. The slopes of the AI peak are well described by Fermi–Dirac (FDD) derivatives (on a log-scale). The peak of the AI is represented by piecewise functions, see Figs. 2–5:

$$\begin{aligned}
&I_{peak}(x) = I_1(x) + I_2(x) + I_3(x) + I_4(x) + I_5(x),\\
&F(x, <x>, A, \sigma) = A \exp\left(c \frac{\exp\left[\frac{x-<x>}{\sigma}\right]}{\left(1+\exp\left[\frac{x-<x>}{\sigma}\right]\right)^2}\right),\\
&I_1 = F(x, x_1, A_2, \sigma_1) \quad x \leqslant x_1,\\
&I_2 = A_2 \exp(c[1/4 + \beta(x - x_1)]) \quad x \in (x_1; x_2],\\
&I_3 = F(x, x_2, A_3, \sigma_2) \quad x \in (x_2; x_3],\\
&I_4 = I_3(x_3) \quad x \in (x_3; x_4],\\
&I_5 = F(x, x_5, A_4, \sigma_2) \quad x \geqslant x_4,\\
&x_5 = x_2 + x_4 - x_3.
\end{aligned} \tag{8}$$

One can see (Figs. 4 and 5) that the slope of the left front (i.e. $I_1$) and the right front ($I_3$ and $I_5$ with the same $\sigma_2$) do not vary with $V_{ds}$. The position of the maxima of $I_1$ and $I_3$($x_1$ and $x_2$, respectively) remains the same with the growing $V_{ds}$ and the only varying parameters are the slope of $I_2$ (parameter $\beta$) and the extension of the ledge $I_4$ (i.e. $x_4 - x_3$); the position of the $I_5$ maximum is linked to the end of $I_4$, see (8). The values of those parameters which vary with the stress $V_{ds}$ (i.e. fitting parameters of the model) are shown in Fig. 3. Their variation with $V_{ds}$ can be represented by a linear dependence. Note that scattering in these parameters is related to the noise in the TCAD data, which is a consequence of the Monte-Carlo method employed for the solution of the Boltzmann transport equation. This circumstance allows to calculate the AI for those stress conditions for which the set of DFs has not been calculated. For this purpose one just needs to interpolate/extrapolate values of $\{A_2, A_3, A_4, \beta, x_4\}$ using the findings from Fig. 3.

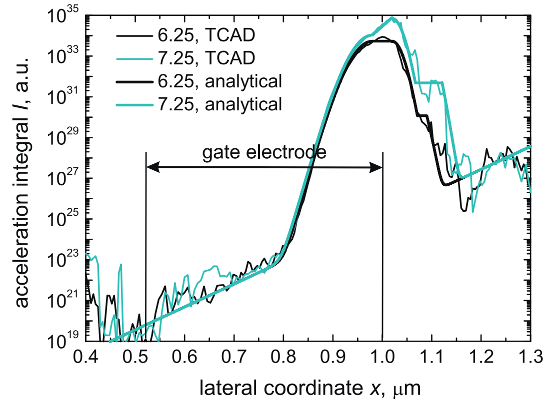


**Fig. 4.** The profile of the acceleration integral: comparison between the AI calculated with the TCAD model and the analytical expression.

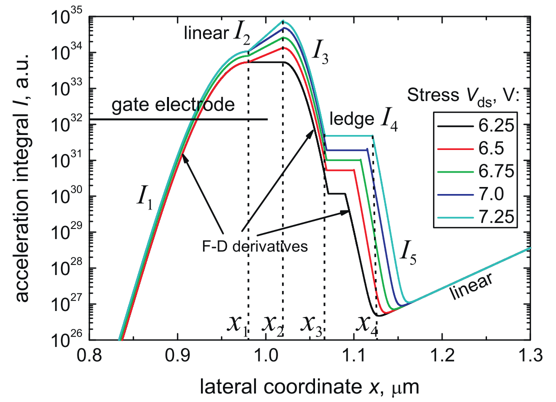


**Fig. 5.** The representation of the AI with the analytical expression for various $V_{ds}$.

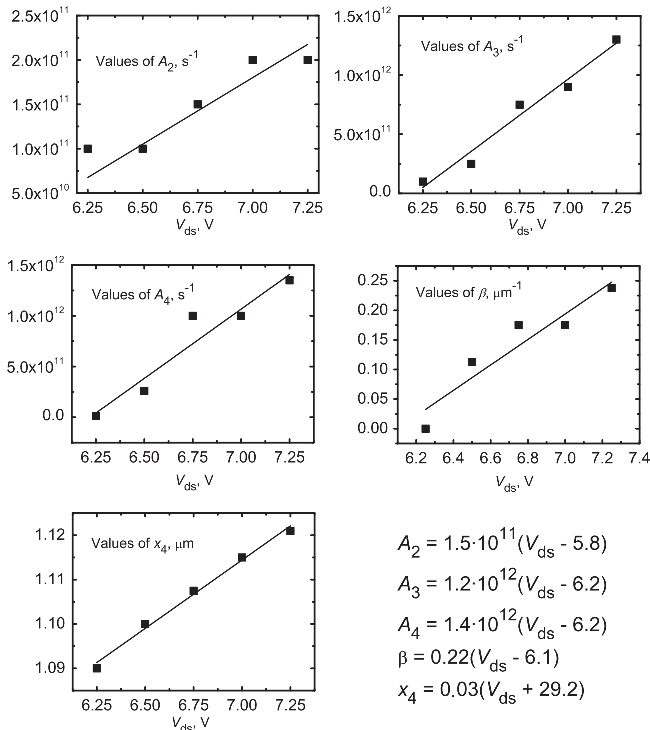


**Fig. 3.** The parameters $A_2$ (a), $A_3$ (b), $A_4$ (c), $\beta$ and $x_4$ vs. $V_{ds}$ as well as their fitting by the linear dependence on $V_{ds}$.

The full solution of (6) is written as

$$\overline{N}_{it,SE} = 1 - (x_{max} - x_{min})^{-1} \sum J_i, \tag{9}$$

where $J_i$ is the contribution produced by the term $I_i$, i.e. $J_i = \int \exp[-\nu t I_i(x)] dx$. The terms $J_i$ are expressed via the exponential integrals of the first kind $Ei_1(x)$ which is defined as [18]:

$$Ei_1(x) = \int_x^\infty \frac{e^{-t}}{t} dt, \ |\arg(x) < \pi|. \tag{10}$$

The contributions $J_i$ have the following structure (terms $J_3$ and $J_5$ are similar to $J_1$ and thus are omitted here):

$$J_1 = \alpha^{-1}\mathrm{Ei}_1(vtA_1\ \exp\ [-\alpha(x - x_{\min})])|_{x_{\min}}^{\tilde{x}},$$
$$\tilde{x} = x_1 + \sigma_1\ \ln\ \frac{1 - 2\tilde{s} - \sqrt{1 - 4\tilde{s}}}{2\tilde{s}}, \tilde{s} = c^{-1}\ln\frac{\ln 2}{vtA_1},$$
$$J_2 = -(c\alpha)^{-1}\mathrm{Ei}_1(vtA_2 \exp(\alpha[1/4 + \beta(x - x_1)]))|_{x_1}^{x_2},$$
$$J_4 = -\alpha^{-1}\exp[-vtI_3(x_1)]\mathrm{Ei}_1(vtA_3 \exp[-\alpha(x - x_0)])|_{x_3}^{x_4}. \quad (11)$$

Fig. 6 demonstrates the time dependences of the integrals $J_i$ calculated for $V_{ds}$ = 7.25 V. The terms $J_i$ reflect the fraction of "virgin" bonds and a decay in $J_i$ means that the dissociation process was triggered during this time slot. One can see that the tip of the AI peak (the term $I_2$ of the AI and the $J_2$ in $\Delta I_{dlin}$) affects $I_{dlin}$ rather weakly already at $t$ = 10 s. In fact, $I_2$ varies approximately in the range of $10^{34}$–$10^{35}$ (Fig. 4) and the criterion $vt\ I_1 \sim 1$ leads to bond-breakage events predominately triggered within the time slot of 0.2–2 s. In contrast, $I_1$ varies by more than 11 orders of magnitude and thus $J_1$ contributes to $\Delta I_{dlin}$ over several decades and defines the degradation at long times. These considerations are summarized in Fig. 7 where the time-dependent values of some terms $J_i$ are substituted by constants. For instance, the term $J_1$ does not substantially change during several decades (Fig. 6) and thus may be represented by the value $J_1(t = 0)$. Fig. 7 shows that during the time slot of 0–$10^4$ s terms $J_2$, $J_3$, $J_5$ are not significant and may be omitted.

Since in the experiment it is impossible to separate the SE-and ME-components, we employed our TCAD model to show the $I_{dlin}$ degradation induced solely by the SE-mechanism. This step is important because it allows to verify the adequacy of the acceleration integral profile representation with a fitting formula. Fig. 8 shows good agreement between results calculated by TCAD and analytical models. The major discrepancy is observed at short times and related to the noise seen in the AI peak and related stochastic nature of the Monte-Carlo method.

Being sure that the SE-component is reasonably represented with the analytical expression we combined SE-and ME-contributions. $\Delta I_{dlin}$ considering also the ME-component is compared with experimental data and plotted in Fig. 9, which demonstrates a very good agreement between simulations and experiment.

This model based on the analytical representation of the AI does not employ time consuming Monte-Carlo simulations required to calculate the set of carrier DFs. One may profit from such an advantage while considering the impact of statistical variations in device geometry (e.g. in the oxide thickness, gate length, etc.) on HCD. If one should recalculate the whole set of carrier DFs with the Monte-Carlo method at each value of the fluctuating parameter, the simulation process will be inadmissibly time expensive. In contrast, within our model the DFs are calculated only once for some reference values of the fluctuating quantity and the fitting parameters of the model (controlling the AI) are defined by interpolation using dependences like Fig. 3. Afterwards, one may use the analytical form of the AI and operate with simple expressions. As a result, we operate with simple expressions which further can be weighted considering the distribution of the fluctuating quantity and statistically processed.

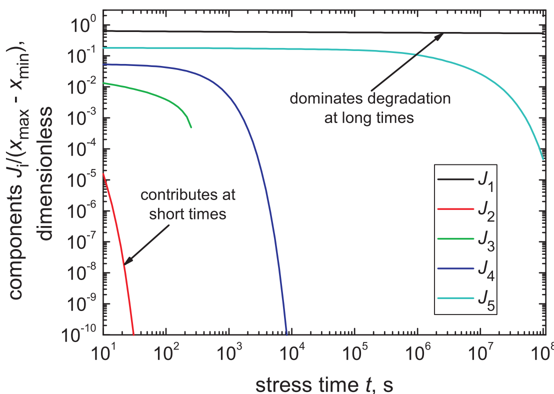


**Fig. 6.** Different contributions to the degradation $J_i$ divided by the gate length for $V_{ds}$ = 7.25 V.

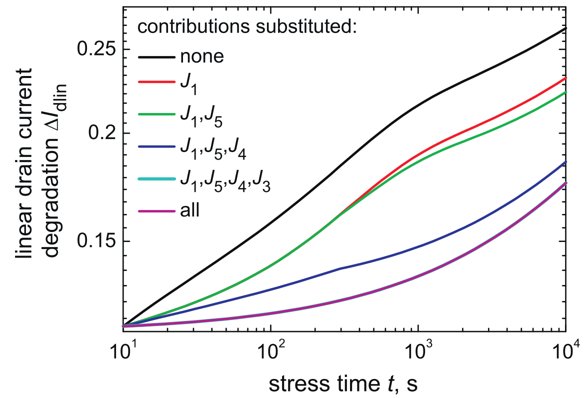


**Fig. 7.** $I_{dlin}$ degradation calculated with substitution of one (or some) contribution (s) $J_i$ by the constant value ($V_{ds}$ = 7.25 V).

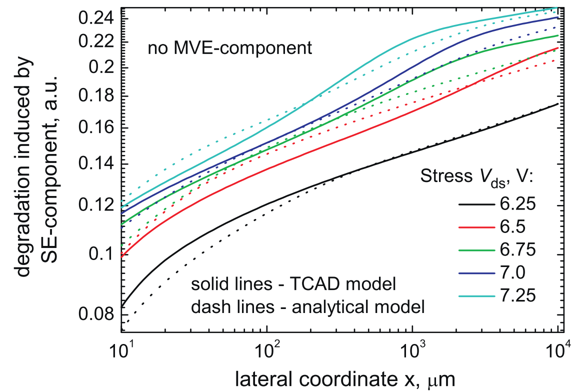


**Fig. 8.** Comparison between the $\Delta I_{dlin}$ portion induced by the SE-component obtained within the TCAD model and the analytical approach.

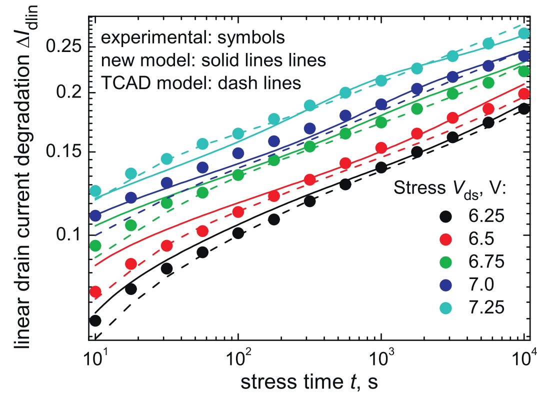


**Fig. 9.** $I_{dlin}$ degradation: experiment vs. simulations. Very good agreement between the experimental data and the results of both TCAD and analytical model is pronounced.

## 4. Conclusions

Based on a rigorous TCAD version of a physics-based model for HCD we have developed an analytical model which suitably approximates the carrier acceleration integral. Using such an approach we are able to represent the linear drain current degradation. Although $\Delta I_{\mathrm{dlin}}$ is expressed as a superposition of exponential integrals one may simplify the solution employing the asymptotics of this special function. For instance, such a simplification is to be done for long times and short time/weak stresses. One of the main advantages of this analytical approach is that it is based on a physics-based TCAD model rather than on an empirical fit to experimental data. Thus, the model captures the superposition of the SE-and ME-process for Si–H bond-breakage and the degradation saturation. This is very important while passing from accelerated stress to real operating conditions which are usually characterized by lower voltages, i.e. one may expect a more pronounced contribution of the ME-component. The model also represents the saturation of HCD observed at relatively long stress times. The flexibility of the resulting expression allows us to employ this approach while considering the impact of fluctuating parameters of device topology on HCD. In this case the time-consuming Monte-Carlo method leads to extremely high computational costs.

## Acknowledgments

This work has received funding from the EC's FP7 Grant agreement No. 216436 (ATHENIS) and from the ENIAC MODERN Project No. 820379.

## References

[1] Hess K, Haggag A, McMahon W, Cheng K, Lee J, Lyding J. The physics of determining chip reliability. Circ Dev Mag 2001:33–8.
[2] McMahon W, Haggag A, Hess K. Reliability scaling issues for nanoscale devices. IEEE Trans Nanotech 2003;2(1):33–8.
[3] Bravaix A, Guerin C, Huard V, Roy D, Roux J, Vincent E. Hot-carrier acceleration factors for low power management in DC–AC stressed 40 nm nmos node at high temperature. In: Proc. international reliability physics symposium (IRPS); 2009. p. 531–46.
[4] Bravaix A, Huard V. Hot-carrier degradation issues in advanced CMOS nodes. In: Proc. European symposium on reliability of electron devices failure physics and analysis (ESREF), tutorial; 2010.
[5] Tyaginov S, Starkov I, Triebl O, Cervenka J, Jungemann C, Carniello S, et al. Hot-carrier degradation modeling using full-band monte-carlo simulations. In: Proc. international symposium on the physical & failure analysis of integrated circuits (IPFA); 2010.
[6] Tyaginov S, Starkov I, Triebl O, Cervenka J, Jungemann C, Carniello S, et al. Interface traps density-of-states as a vital component for hot-carrier degradation modeling. Microelectron Reliab 2010;50:1267–72.
[7] Haggag A, McMahon W, Hess K, Cheng K, Lee J, Lyding J. High-performance chip reliability from short-time-tests. statistical models for optical interconnect and HCI/TDDB/NBTI deep-submicron transistor failures. In: Proc. international reliability physics symposium (IRPS); 2001. p. 271–9.
[8] McMahon W, Matsuda K, Lee J, Hess K, Lyding J. The effects of a multiple carrier model of interface states generation of lifetime extraction for MOSFETS. In: Proc. int. conf. mod. sim. micro, vol. 1; 2002. p. 576–9.
[9] Grasser T, Reisinger H, Wagner PJ, Kaczer D, Schanowsky F, Gös W. The time dependent defect spectroscopy (TDDS) for the characterization of the bias temperature instability. In: Proc. international reliability physics symposium (IRPS); 2010. p. 16–25.
[10] Reisinger H, Grasser T, Schlunder C, Gustin W. The statistical analysis of individual defects constituting NBTI and its implications for modeling DC- and AC-stress. In: Proc. international reliability physics symposium (IRPS); 2010. p. 7–15.
[11] Kaczer B, Grasser T, Roussel P, Franco J, Degraeve R, Ragnarsson L, et al. Origin of NBTI variability in deeply scaled pFETs. In: Proc. international reliability physics symposium (IRPS); 2010. p. 26–32.
[12] Huard V, Denais M, Perrier F, Revil N, Parthasarathy C, Bravaix A, et al. A thorough investigation of mosfets NBTI degradation. Microelectron Reliab 2005;45:83–98.
[13] Bindu B, Goes W, Kaczer B, Grasser T. Analytical solution of the switching trap model for negative bias temperature stress. In: Proc. international integrated reliability workshop (IIRW); 2009. p. 93–6.
[14] Jungemann C, Meinerzhagen B. Hierarchical device simulation. Wien/New York: Springer Verlag; 2003.
[15] Wong H-S, White M, Krutsick J, Booth R. Modeling of transconductance degradation and extraction of threshold voltage in thin oxide MOSFET's. Solid-State Electron 1987;30(9):953–8.
[16] Stojadinovic N, Pejovic M, Golubovic S, Ristic G, Davidovic V, Dimitriev S. Effect of radiation-induced oxide-trapped charge on mobility in p-channel MOSFETs. Electron Lett 1995;31(6):497–8.
[17] Prakash AG, Ke S, Siddappa K. High-energy radiation effects on subthreshold characteristics, transconductance and mobility of n-channel MOSFETs. Semicond Sci Technol 2003;18(12):1037–42.
[18] Abramowitz M, Stegun I. Handbook on mathematical functions. New York: Dover; 1972.